AGU PUBLICATIONS

Journal of Advances in Modeling Earth Systems

RESEARCH ARTICLE

10.1002/2017MS001059

Vertical Velocity in the Gray Zone

Nadir Jeevanjee[1,2]

[1]Program in Atmosphere and Ocean Sciences, Princeton University, Princeton, NJ, USA, [2]Geophysical Fluid Dynamics Laboratory, Princeton, NJ, USA

Key Points:
- Horizontal resolutions of $O(100\,\mathrm{m})$ can be required for convergence of convective vertical velocities w_c
- Hydrostatic systems overestimate w_c, by a factor of 2–3 at fine resolution
- This overestimation can be simply understood using the notion of "effective buoyancy pressure"

Supporting Information:
- Supporting Information S1
- Movie S1

Correspondence to:
N. Jeevanjee,
nadir.jeevanjee@noaa.gov

Citation:
Jeevanjee, N. (2017). Vertical velocity in the gray zone. *Journal of Advances in Modeling Earth Systems*, *9*. https://doi.org/10.1002/2017MS001059

Received 23 MAY 2017
Accepted 2 SEP 2017
Accepted article online 7 SEP 2017

Abstract We describe how convective vertical velocities w_c vary in the "gray zone" of horizontal resolution, using both hydrostatic and nonhydrostatic versions of GFDL's FV^3 dynamical core, as well as analytical solutions to the equations of motion. We derive a simple criterion (based on parcel geometries) for a model to resolve convection, and find that $O(100\,\mathrm{m})$ resolution can be required for convergence of w_c. We also find, both numerically and analytically, that hydrostatic systems overestimate w_c, by a factor of 2–3 in the convection-resolving regime. This overestimation is simply understood in terms of the "effective buoyancy pressure" of Jeevanjee and Romps (2015, 2016).

1. Introduction

As computer power increases, so does the maximum resolution of atmospheric models. Indeed, it is now possible to run global climate simulations at subdegree horizontal resolution (Noda et al., 2014; Wehner et al., 2014), and shorter-term numerical weather prediction simulations at $O(1\mathrm{km})$ resolution (Kain et al., 2008; Lean et al., 2008; VandenBerg et al., 2014). Such resolutions lie outside both the hydrostatic regime, wherein resolved-scale convective vertical velocities w_c are negligible, as well as the convection-resolving regime, wherein w_c converge to constant, realistic values.

This no-man's land of horizontal resolution is sometimes known as the "gray zone" (Figure 1). In the gray zone, the vertical transports of heat, moisture, and other tracers by the resolved-scale motion can be neither neglected nor relied upon, and are expected to vary strongly as a function of resolution. Indeed, the structure of atmospheric circulations at a variety of scales, as well as the utility of convective parameterizations, are known to vary significantly within the gray zone (Prein, 2015; Wehner et al., 2014; Weisman et al., 1997, hereafter W97). This raises difficult and important questions about when to turn convective parameterizations off, and/or how to make them "scale-aware." Since these issues are all tied to w_c, and since w_c is relevant for both climate forcing and sensitivity (Donner et al., 2016), it seems worthwhile to address some basic questions about the behavior of w_c in the gray zone:

1. For a given dynamical phenomenon, at what resolution should one expect the associated w_c to converge? In other words, where is the inner edge of the gray zone?
2. If w_c converges at fine resolutions and is negligible at coarse resolutions, what kind of curve interpolates between these two regimes?
3. If hydrostatic models are used in the gray zone, how might their behavior differ from their nonhydrostatic counterparts, and how can we understand such differences?

Questions 1 and 2 are depicted schematically by the question marks in Figure 1.

This paper seeks to address these questions through both analytical solutions to the relevant equations of motion as well as cloud-resolving numerical simulations, run with an atmospheric model equipped with both hydrostatic and nonhydrostatic solvers. Of course, similar approaches have been taken by previous authors (W97; Kato & Saito, 1995; Morrison, 2016b; Orlanski, 1981; Pauluis & Garner, 2006), so we must build on these prior studies in meaningful ways. We do so by first taking advantage of the aforementioned computer power to explore much finer resolutions ($dx \lesssim 100\,\mathrm{m}$) than these previous studies ($dx \gtrsim 2$ km), ideally probing down to the inner edge of the gray zone. Second, we use a postprocessing algorithm to diagnose the diameter D and vertical extent (or height) H of individual convecting parcels in our simulations, to explicitly make the connection between parcel geometry and resolution. Third, we apply the recently developed "effective buoyancy" formalism (Davies-Jones, 2003; Jeevanjee & Romps, 2015) to develop scaling laws for both hydrostatic and

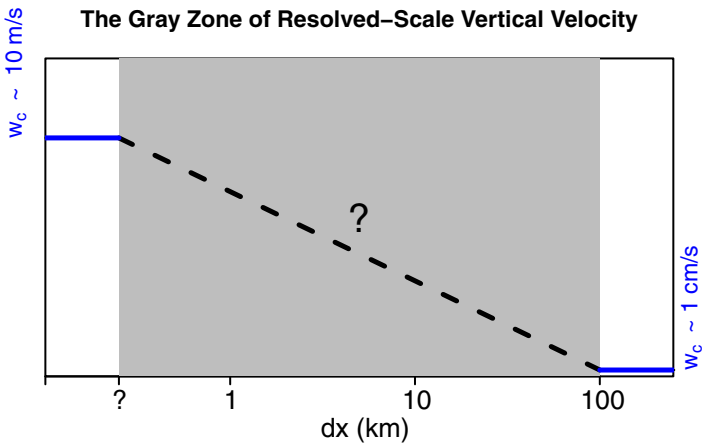

Figure 1. Schematic depiction of the gray zone. At some unknown fine resolution, we expect convective vertical velocities w_c to converge to a realistic typical value, and at very coarse resolution we expect w_c to become negligible, but it is unclear how to interpolate between these two regimes.

nonhydrostatic vertical velocities, and we compare these to previously published scalings. Finally, we will reemphasize the perhaps counterintuitive fact that hydrostatic systems *over*estimate w_c. This fact is noted in the references listed above, but perhaps deserves fresh emphasis as computer power allows global hydrostatic models to be run in the gray zone. We will also give intuition for this overestimation using the "buoyancy pressure" framework of Jeevanjee and Romps (2015, 2016; hereafter JR15 and JR16, respectively).

Our focus here will be on the effects of horizontal resolution on parcel aspect ratio D/H and hence vertical acceleration, as opposed to the effects of horizontal resolution on turbulence and entrainment (e.g., Bryan et al., 2003; Bryan & Morrison, 2011; Lebo & Morrison, 2015; Wyngaard, 2004). These effects are likely related, though, as Lebo and Morrison (2015) find that the onset of resolved turbulent mixing *and* the convergence of vertical motion coincide at $dx = 250$ m. This gives a tentative answer to question 1 above, but the answer is purely empirical. A further aim of this paper will be to develop a criterion for resolving convection which reproduces this result (section 3), and explains it in terms of other phenomenological parameters of our simulations.

2. Simulations

We begin by probing the gray zone numerically. This task requires an atmospheric model which can run with both hydrostatic and nonhydrostatic solvers while keeping other model components fixed (such as the horizontal advection scheme and physics parameterizations). To that end, we employ a dynamical core with just such a capability, GFDL's FV^3 (Finite-Volume Cubed-Sphere Dynamical Core) (Harris & Lin, 2013; Lin, 2004). Global nonhydrostatic convection-allowing simulations with FV^3-based models have been done for some time, with both GFDL's HiRAM (https://www.gfdl.noaa.gov/visualizations-mesoscale-dynamics/) and NASA GEOS (Putman & Suarez, 2011), but this paper marks the debut of FV^3 in subkilometer, doubly periodic cloud-resolving simulations. We will confirm its suitability for this application below.

As for the model configuration and physics, our guiding principle is to avoid inessential complexity insofar as possible (Jeevanjee et al., 2017). Thus, we choose to run simple doubly periodic radiative-convective equilibrium (RCE) simulations over a fixed sea surface temperature of 300 K, using bulk aerodynamic surface fluxes with a fixed drag coefficient of 1.5×10^{-3}, along with an imposed gustiness of 5 m/s to obtain the small air-sea temperature difference typical of the tropics. Radiative cooling is noninteractive and fixed at 1 K/d between the surface and 150 hPa, above which temperatures are relaxed to a stratospheric target of 200 K over a timescale of 5 days. Above 100 hPa, we introduce a Rayleigh drag on the horizontal winds with a 1/2 day timescale to act as a sponge for upwelling gravity waves. No boundary layer or subgrid turbulence schemes are used, though small amounts of vorticity and divergence damping are used to stabilize the model and reduce noise. Microphysical transformations are performed by the six-category GFDL microphysics scheme (Chen & Lin, 2013). The vertical discretization is Lagrangian (Lin, 2004) with 151 levels, with spacings ranging smoothly from 4 hPa near the surface to 8 hPa in the midtroposphere, and back down to 4 hPa near the model top at 76 hPa. The horizontal grid has 96 points in both x and y.

Simulations were run at resolutions spanning $dx = 0.0625 - 16$ km, varying by factors of two, in both hydrostatic and nonhydrostatic mode. We initially spun up a nonhydrostatic $dx = 2$ km simulation for 480 days to attain full equilibration (i.e., no discernible temperatures or moisture trends) throughout the whole domain (including the stratosphere), and then branched all other runs off this run, running for at least 60 days to allow adjustment to different resolutions or the hydrostatic solver. Three-dimensional snapshots were saved daily from these runs, and the last 20 days of such output were fed into an algorithm which identified convecting parcels and diagnosed their diameter D, height H, and vertical velocity w_c. The algorithm identifies parcels as maxima in w, then identifies the associated maxima in Archimedean buoyancy B, and then identifies parcel dimensions D and H via a B threshold (see Appendix C for details). Averaging over all tracked

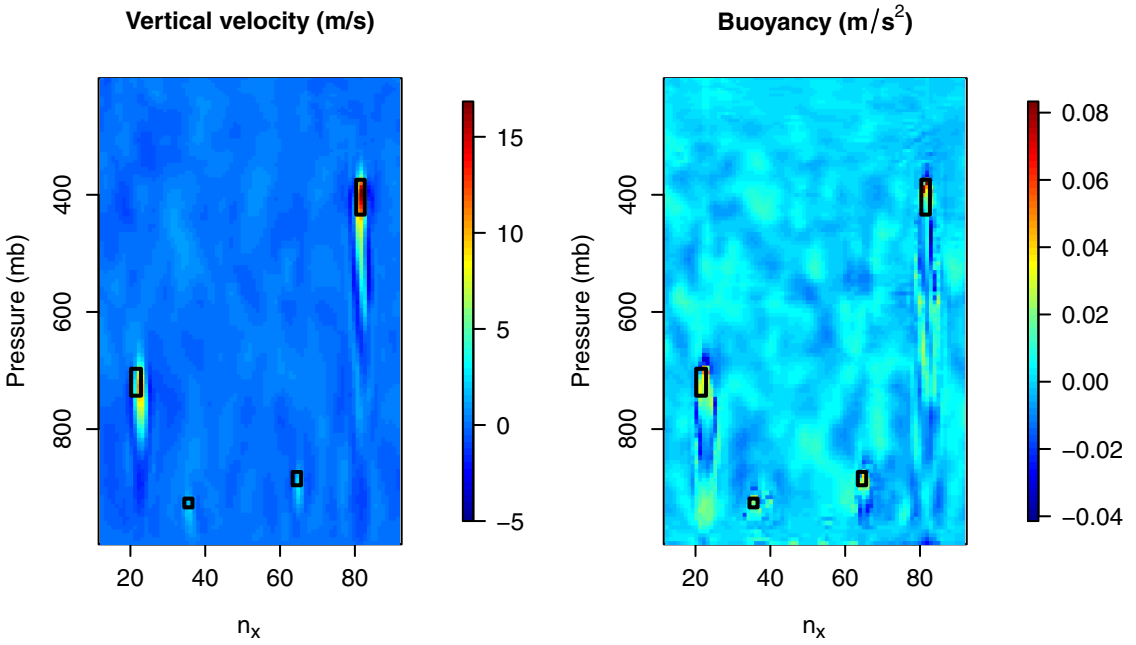

Figure 2. $x - p$ slices of vertical velocity and Archimedean buoyancy from our nonhydrostatic, $dx = 0.25$ km simulation. This slice contains several parcels that were identified by the algorithm, and the diagnosed horizontal and vertical extent of the parcels are depicted via black boxes (some parcels have their B maxima in adjacent $x - p$ slices and so do not appear perfectly centered within their box). Note that the parcel extent is defined by the B field, not the w field, which typically has a larger vertical extent than the B field. Only part of the full $x - p$ domain is shown. n_x denotes grid cell number in the x-direction.

parcels then yields characteristic values of D, H, and w_c for a given simulation, which are used in our analysis below.

To get a feel for these simulations (as well as the diagnostic algorithm), and to show that the FV^3 dynamical core and GFDL microphysics can indeed handle the transition from coarser-resolution general circulation calculations to subkilometer cloud-resolving calculations, $x - p$ slices of vertical velocity w and Archimedean buoyancy B from our nonhydrostatic, $dx = 0.25$ km simulation are shown in Figure 2. (An animation of the cloud field is given in Movie S1.) The features in these fields seem reasonable, being comparable to those found in simulations we have run with other cloud-resolving models, such as DAM (Romps, 2008, not shown). The slice in Figure 2 contains several parcels that were identified by the diagnostic algorithm, and their diagnosed horizontal and vertical extents are depicted by black boxes drawn around the parcels (some parcels have their B maxima in adjacent $x - p$ slices and so do not appear perfectly centered within their box). Note that parcel w fields typically have a significantly larger vertical extent than their B fields, and that neither of these fields extend down to the ground, contravening the simple "plume" picture of convection prevalent in convective parameterizations (e.g., Arakawa & Schubert, 1974).

3. Criterion for the Convection-Resolving Regime

We begin our analysis by addressing the first question from the introduction, namely: where is the inner edge of the gray zone? To answer this, we must first define the gray zone (for a given model configuration). We define it here, somewhat loosely, to be those horizontal resolutions at which a model's convective parameterizations might be credibly turned off, but at which resolved-scale convection is still *grid-limited*, in the sense that the physical size of convecting parcels is not independent of dx, but rather scales directly with it. Thus, in the gray zone the diameter D of convecting parcels varies as

$$D = n_{\text{gray}}\, dx\,, \qquad (\text{gray zone}) \tag{1}$$

for fixed n_{gray}. This is, of course, merely a definition; we must check whether a gray zone defined this way, with a corresponding n_{gray}, exists for our simulations. This is done in Figure 3a, which plots the average parcel width (measured in grid cells) $n \equiv D/dx$ for both our hydrostatic and nonhydrostatic simulations. This

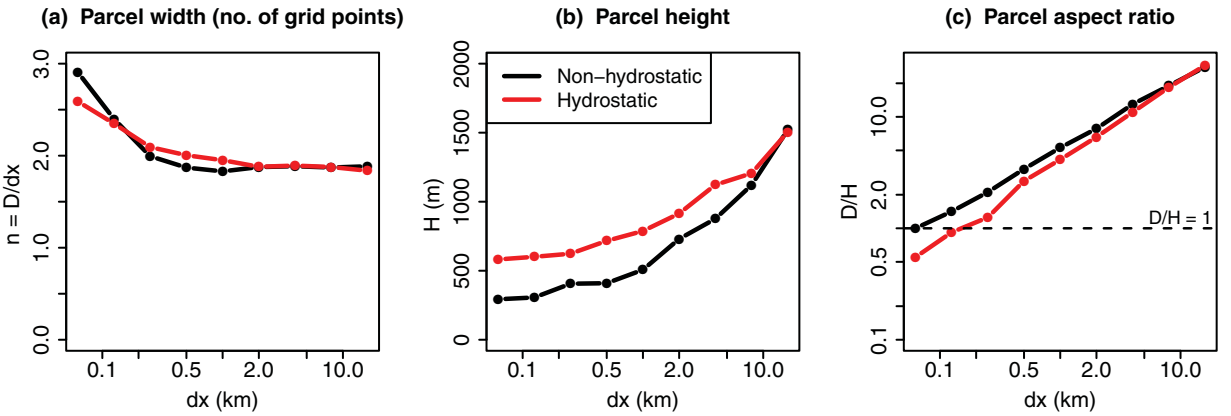

Figure 3. Average parcel properties, diagnosed using the algorithm discussed in Appendix C, as a function of resolution dx, for both hydrostatic and nonhydrostatic RCE simulations. (a) Parcel diameter measured in number of grid cells, $n=D/dx$. This is fairly constant at $n_{gray} \approx 2$ for $dx > 250$ m, and starts to increase for $dx \lesssim 250$ m, marking the inner edge of the gray zone. (b) Parcel height H, which is fairly constant at roughly 500 m for $dx \lesssim 250$ m. (c) Aspect ratio D/H, which reaches the neighborhood of ~ 1 around $dx = 0.125$ km.

plot shows that such a gray zone indeed exists for $dx > 250$ m, where $n = n_{gray} \approx 2$, and that $n > n_{gray}$ for $dx \lesssim 250$ m.

Why does the gray zone end at $dx \approx 250$ m? In the convection-resolving regime we have

$$D > n_{gray}\, dx\,, \qquad (\text{convection}-\text{resolving}) \tag{2}$$

which is just another way of saying that convection is no longer grid-limited. In the convection-resolving regime, we also expect that

$$D/H \approx 1 \qquad (\text{convection}-\text{resolving}) \tag{3}$$

since recent high-resolution simulations as well as older observations show that convecting parcels resemble spherical "thermals" (Hernandez-Deckers & Sherwood, 2016; Romps & Charn, 2015; Scorer, 1957; Woodward, 1959). This is confirmed in Figure 3c, which plots average parcel aspect ratio (where D/H is computed individually for each parcel before averaging) and shows that $D/H \approx 1$ at high resolutions (it is unclear why D/H is closer to 0.5 at $dx = 0.0625$ km for the hydrostatic simulation, though it may be related to the asymmetry between vertical and horizontal motion discussed in section 5). Putting facts (2) and (3) together yields the following inequality for the convection-resolving regime, which also demarcates the inner edge of the gray zone:

$$dx < H/n_{gray}\,. \qquad (\text{convection}-\text{resolving}) \tag{4}$$

This simple inequality provides a tentative answer to question 1 posed in the introduction. To evaluate it, we need to know the vertical extent H of our parcels. This is plotted in Figure 3b, which shows that H has some resolution dependence, but asymptotes to roughly 500 m at fine resolution. Plugging $H = 500$ m and $n_{gray} = 2$ into equation (4) yields $dx = 250$ m for the inner edge of the gray zone, in good agreement with Figure 3a as well as Lebo and Morrison (2015).

Equation (4) thus seems to capture the edge of the gray zone, as we have defined it. But, this equation is only relevant to the questions posed in the introduction and by Figure 1 if parcel vertical velocities w_c converge according to the same criterion. We thus plot average parcel w_c for our simulations in Figure 4. This plot shows that for the nonhydrostatic solver, w_c indeed converges around $dx = 250$ m, in agreement with Equation (4). Note that in the convection-resolving regime of $dx \lesssim 250$ m we expect more turbulence with higher resolution, but the small variations of w_c in this regime suggest that the impact of this on vertical velocities is not strong.

While the convergence of w_c at the resolution predicted by (4) is reassuring, the much more striking feature of Figure 4 is the *over*estimation of w_c by the hydrostatic solver, by a factor of 2–3 in the convection-resolving regime (see also W97). We also still lack understanding about the overall shape of the

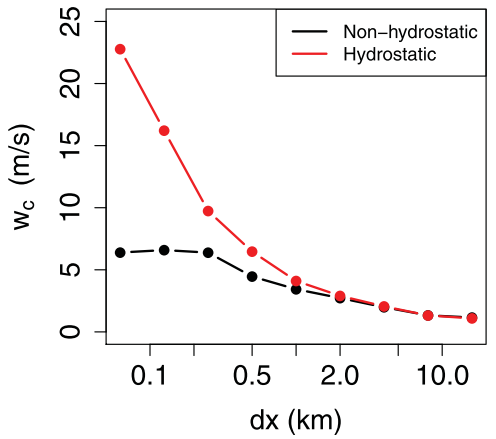

Figure 4. Convective vertical velocities w_c as a function of resolution dx, for both hydrostatic and nonhydrostatic RCE simulations. Note that w_c values appear to converge for $dx \lesssim 250$ m, roughly consistent with equation (4). Note also that the hydrostatic solver indeed overestimates w_c, by a factor of about 2–3 for $dx \lesssim 250$ m.

nonhydrostatic w_c curve and how it interpolates between the hydrostatic ($D/H \gg 1$) and convection-resolving ($D/H \approx 1$) limit. We investigate these questions analytically in the next section.

4. The Shape of $w_c(dx)$

4.1. Hydrostatic and Nonhydrostatic Effective Buoyancy

To understand the shape of $w_c(dx)$, we must understand the resolution-dependence of the forces that act on convecting parcels. Since convection is by definition a buoyancy-driven flow, we will focus here on the "effective buoyancy" β, defined as (JR15)

$$\beta \equiv \left.\frac{dw}{dt}\right|_{\mathbf{u}=0}. \tag{5}$$

This definition applies to both hydrostatic and nonhydrostatic systems, and gives the net vertical acceleration due to density anomalies. By setting the wind field $\mathbf{u}=0$, the effective buoyancy neglects the "dynamic" pressure gradients arising from advection of momentum or inertia (JR15; Markowski & Richardson, 2011, hereafter MR11). We will return to possible effects of this approximation in section 6.

The effective buoyancy β is typically understood as a combination of the Archimedean buoyancy B along with a "buoyancy perturbation pressure" gradient which offsets B (MR11). This offset is almost total when $D/H \gg 1$ (Morrison, 2016a, hereafter M16), which is why global model grid cells typically do not convect efficiently and convection must be parameterized. The perturbation pressure formalism is not well-suited to analyze hydrostatic systems, however, because the perturbation pressure contains both hydrostatic and nonhydrostatic components (M16, MR11).

Instead, we employ the formalism of Das (1979), which splits the total pressure into the *local* hydrostatic pressure $p_{\mathrm{hyd}} \equiv \int_z^\infty \rho g\, dz'$ and a residual nonhydrostatic pressure p_{nh}. Applying (5) within this formalism to a nonhydrostatic, Boussinesq fluid with reference density ρ_0 yields the following equation for the nonhydrostatic effective buoyancy β_{nh} (JR16):

$$-\nabla^2 \beta_{\mathrm{nh}} = -\nabla_{\mathrm{h}}{}^2 B\,. \tag{6}$$

Here B is given by the usual formula $B \equiv g(\rho_0 - \rho)/\rho_0$, and the horizontal Laplacian is (crucially) $\nabla_{\mathrm{h}}{}^2 \equiv \partial_x{}^2 + \partial_y{}^2$. We will present intuition for β_{nh} in section 5. Also note that (6) is incomplete without boundary conditions, which can be derived from boundary conditions on w. In this paper, we assume a surface at $z = 0$, at which $w \equiv 0$, and this implies $\beta \equiv 0$ there as well (JR15). We also assume that w (and hence β) go to 0 as $z \to \infty$.

What is the analog of equation (6) for a hydrostatic system? In the hydrostatic approximation, we know that w is given diagnostically from the mass continuity equation by (e.g., Adcroft et al., 2011, Figure 1.17)

$$w = -\int_0^z dz'\, \nabla_{\mathrm{h}} \cdot \mathbf{V} \tag{7}$$

where $\mathbf{V} = (u, v)$ is the horizontal wind field. Taking the time-derivative of both sides, and applying the nonrotating hydrostatic momentum equation $\rho_0\, d\mathbf{V}/dt = -\nabla_{\mathrm{h}} p_{\mathrm{hyd}}$ along with (5), gives

$$\beta_{\mathrm{hyd}} = \int_0^z dz'\, \frac{1}{\rho_0} \nabla_{\mathrm{h}}{}^2\, p_{\mathrm{hyd}}\,. \tag{8}$$

This is the equation for hydrostatic effective buoyancy. Note that applying $\partial_z{}^2$ to equation (8) yields equation (6), if one neglects the horizontal Laplacian (as is appropriate in the hydrostatic limit).

Equations (6) and (8) only determine β once horizontal density anomalies or an Archimedean buoyancy field are specified, so we now specify this source field. This source field should have not only a characteristic

Archimedean buoyancy B_0 and characteristic width D, but also a characteristic height H, since it is only in relation to H that D gets large (for an atmospheric model, H is bounded by the roughly 10 km height of the troposphere, whereas D can easily be an order of magnitude larger). Since we will be interested in parcels for which D may be comparable to their height above the surface (in which case they will feel the effects of the surface boundary condition, JR16), and since the diagnostic equation (8) only makes sense in the presence of a lower boundary, we place our source field directly above the surface. Finally, for simultaneous tractability of both equations (6) and (8), we take the source field to be doubly periodic in both x and y. Putting these specifications together gives the Archimedean buoyancy source field

$$B=\begin{cases} 0 & z > H \\ B_0 \cos\left(\frac{\pi x}{D}\right)\cos\left(\frac{\pi y}{D}\right) & z < H \end{cases}. \tag{9}$$

The resulting effective buoyancy fields $\beta_{\text{hyd}}(\mathbf{x})$ and $\beta_{\text{nh}}(\mathbf{x})$ will also be doubly periodic, and what we seek are their amplitudes β_{hyd} and β_{nh}, evaluated at $z=H/2$, as a function of D, H, and B_0 (we overload the symbols β_{hyd} and β_{nh} here slightly). These are derived in Appendix A. We find that β_{hyd} and β_{nh} are functions of D and H only in their ratio D/H, and are given by

$$\beta_{\text{nh}}(D/H)=B_0\left[1-\frac{1}{2}e^{-\frac{\pi H}{\sqrt{2}D}}\left(3-e^{-\frac{\sqrt{2}\pi H}{D}}\right)\right] \tag{10a}$$

$$\beta_{\text{hyd}}(D/H)=B_0\frac{3\pi^2}{4}\frac{H^2}{D^2}. \tag{10b}$$

As a quick check of these results, one can Taylor-expand (10a) to lowest order in the hydrostatic limit $D/H \gg 1$, and find it exactly equal to (10b). Also note that both expressions in (10) go to 0 in this limit, as expected. In the $D/H \to 0$ limit β_{nh} approaches B_0, also as expected, and β_{hyd} diverges. It is not clear if this latter behavior should actually be realized in hydrostatic models, however, because once a given phenomenon is well resolved D ceases to scale with dx, just as we find here (Figure 3a).

4.2. A Scaling for w_c

With expressions for β in hand, we now need to relate β to the convective vertical velocity w_c. The relationship between these two quantities is not entirely settled, though two paradigms exist. One, known as the "slippery thermal" paradigm (Sherwood et al., 2013), employs the work-energy theorem and assumes that (effective) buoyancy is the dominant force on convecting parcels. This paradigm relates β and w_c as

$$w_c^2/2 = \beta\Delta z \tag{11}$$

where Δz gives the height range over which the effective buoyancy β has acted.

The other paradigm, known as the "sticky thermal" paradigm (Romps & Charn, 2015), says that convecting parcels usually rise at a terminal velocity determined by a balance between (effective) buoyancy and drag:

$$\rho C_d A w_c^2/2=\rho V\beta \tag{12}$$

where C_d is a drag coefficient, A is the horizontal area of the parcel, and V its volume.

Though these two paradigms are not physically consistent, they are equivalent for our purposes, in that both equations (11) and (12) imply that $w_c \sim \sqrt{\beta}$. If we now define w_{c0} as the limit of nonhydrostatic w_c as $D/H \to 0$, and recall that $\beta_{\text{nh}} \to B_0$ in this limit, we then obtain the following scaling law for w_c as a function of D/H:

$$\frac{w_c}{w_{c0}} = \sqrt{\beta/B_0}. \tag{13}$$

Here, β is evaluated using equations (10a) and (10b), and the resulting scalings are plotted in Figure 5. The nonhydrostatic curve interpolates from the convection-resolving regime ($D/H \lesssim 1$) through the gray zone to the hydrostatic regime ($D/H \gg 1$), where the hydrostatic and nonhydrostatic solutions agree. These two curves also bear a qualitative similarity to the simulated $w_c(dx)$ in Figure 4. We can test the qualitative accuracy of equation (13) by plotting the simulated w_c/w_{c0} against the corresponding D/H, as shown by the stars in Figure 5. (For the simulations, w_{c0} is determined by a least-squares fit of $\sqrt{\beta_{\text{nh}}/B_0}$ to the

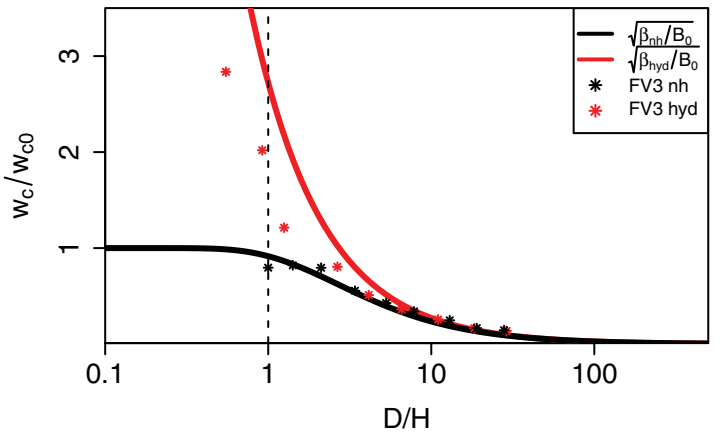

Figure 5. Plots of $w_c/w_{c0}=\sqrt{\beta/B_0}$, where β as a function of D/H is given by equation (10). The nonhydrostatic curve interpolates from the convection-resolving regime ($D/H \approx 1$) through the gray zone to the hydrostatic regime ($D/H \gg 1$), where the hydrostatic and nonhydrostatic solutions agree. Also shown are the simulated w_c/w_{c0}, plotted against the diagnosed D/H (w_{c0} is determined by a least-squares fit of $\sqrt{\beta_{nh}/B_0}$ to the nonhydrostatic w_c points). The nonhydrostatic scaling does a good job overall of capturing the simulated $w_c(D/H)$, while the hydrostatic scaling is somewhat of an overestimate. Note, however, that the hydrostatic scalings and simulations both overestimate their hydrostatic counterparts by a factor of 2–3 for $D/H \lesssim 1$.

nonhydrostatic w_c.) The nonhydrostatic scaling does a good job overall of capturing the simulated $w_c(D/H)$, while the hydrostatic scaling is an overestimate but roughly captures the factor of 2–3 discrepancy in the convection-resolved regime found in Figure 4. These scalings perform comparably to previously published scaling laws, as shown in Appendix B.

5. Intuition for $\beta_{hyd}>\beta_{nh}$

The scalings plotted in Figure 5 seem to roughly capture the simulated overestimation of vertical velocities by the hydrostatic solver. But, why does this overestimation occur? Why should the hydrostatic approximation, in which β is actually *neglected* in the vertical momentum equation, *over*estimate β? Note that it is possible to have $\beta_{hyd} > B$ (Figure 5), so this overestimation cannot be explained by assuming that the hydrostatic approximation neglects the buoyancy perturbation pressure (which it does not, since the buoyancy perturbation pressure has both hydrostatic and nonhydrostatic components).

To proceed we turn to the "effective buoyancy pressure," which was defined in JR15 as simply the nonhydrostatic pressure field that results when $\mathbf{u}=0$:

$$p_\beta \equiv p_{nh}|_{\mathbf{u}=0} \tag{14}$$

(note the analogy to equation (5)). From this it can be shown (JR15) that p_β obeys the equation

$$-\nabla^2 p_\beta = \nabla_h{}^2 p_{hyd}\,, \tag{15}$$

which just says that $-\nabla p_\beta$ must generate a mass divergence which cancels that from $-\nabla_h p_{hyd}$, which is the only gravitational term in the momentum equation in this formalism. By taking $-\partial_z$ of equation (15) and comparing to (6), it is straightforward to show that

$$\beta_{nh} = -(\partial_z p_\beta)/\rho_0\,, \tag{16}$$

i.e., *the nonhydrostatic effective buoyancy is simply the vertical gradient of the effective buoyancy pressure*. Note that p_β was dubbed the "buoyancy pressure": in JR15, but we refer to it here as the "effective buoyancy pressure" to help distinguish it from the buoyancy perturbation pressure mentioned above.

Some intuition for equations (15) and (16) is given in the right plot of Figure 6, as follows: a positively buoyant parcel produces an anomalous hydrostatic pressure field $p'_{hyd} < 0$, whose horizontal gradients force

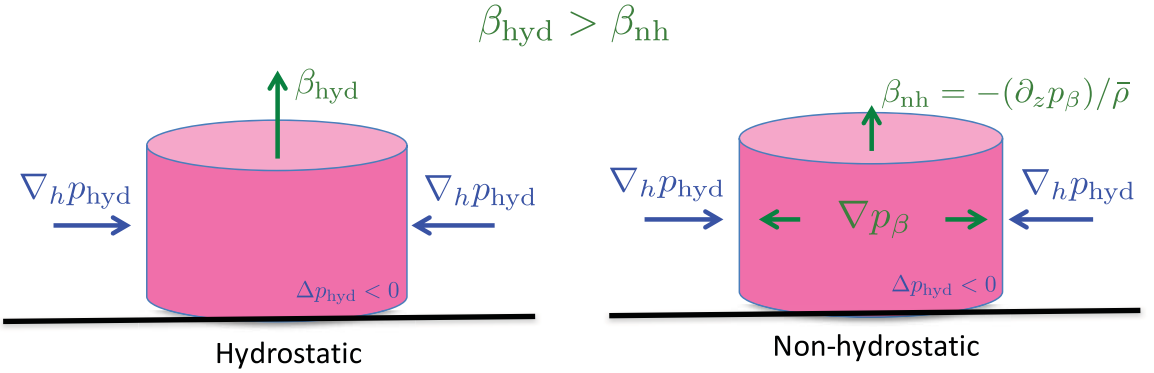

Figure 6. Cartoon of how density-driven vertical accelerations are generated in both the nonhydrostatic and hydrostatic equations of motion (right and left plots, respectively). In the nonhydrostatic formulation the vertical acceleration β_{nh} need only compensate for the *net* horizontal convergence between $-\nabla_h p_\beta$ and $-\nabla_h p_{hyd}$, whereas in the hydrostatic approximation β_{hyd} must compensate for the *gross* convergence from $-\nabla_h p_{hyd}$, with no offset from $-\nabla_h p_\beta$. Thus, $\beta_{hyd} > \beta_{nh}$.

mass convergence into the parcel. This convergence must be compensated for by gradients of the countervailing *non*hydrostatic effective buoyancy pressure p_β. Figure 6 shows that for a surface parcel, p_β responds to horizontal convergence from $-\nabla_h p_{hyd}$ by generating both horizontal and vertical divergence to compensate, and the vertical divergence is given essentially by β_{nh}. Although there is no Archimedean buoyancy in this picture, it is not as unfamiliar as it may seem, as this is just the typical way we understand the operation of a chimney: horizontal p_{hyd} gradients force vertical acceleration via mass continuity. Also note that the divergence from β_{nh} needs only to compensate for the *net* convergence in the horizontal, which exhibits a partial cancellation between $-\nabla_h p_\beta$ and $-\nabla_h p_{hyd}$.

With this picture of convection in hand, JR16 showed that the vertical length scale over which p_β declines from parcel center scales with D, which explains why β decreases with increasing D/H (a similar explanation was given in Pauluis & Garner, 2006). Here, we use this picture to understand why $\beta_{hyd} > \beta_{nh}$, by considering its hydrostatic analog, illustrated in the left plot of Figure 6. In the hydrostatic approximation, nonhydrostatic pressures such as p_β are 0, and the vertical acceleration β_{hyd} is then defined by the requirement that it enforce mass continuity, as in equation (8). In this case, however, β_{hyd} must compensate for the *gross* convergence from $-\nabla_h p_{hyd}$, with no offset from $-\nabla_h p_\beta$. It then follows that

$$\beta_{hyd} > \beta_{nh} ,$$

i.e., that the hydrostatic approximation overestimates vertical accelerations.

The essential reason for this is as follows. In the anelastic or Boussinesq governing equations, mass continuity is enforced by nonhydrostatic pressure fields, which generate divergence in all dimensions. In the hydrostatic approximation, on the other hand, mass continuity is enforced by simply demanding that vertical divergence cancel any horizontal divergence (equation (7)). Thus, in hydrostatic systems the entire burden of mass conservation falls on the *vertical* motion, which is then exaggerated relative to nonhydrostatic vertical motion.

6. Summary and Discussion

We summarize our results as follows:

1. For a model with characteristic parcel height H and gray zone grid cell width n_{gray}, the convection-resolving regime requires $dx < H/n_{gray}$. For our FV^3 simulations, this translates to $dx \lesssim 250$ m (Figures 3 and 4).
2. Hydrostatic solvers seem to overestimate w_c by a factor of 2–3 in the convection-resolving regime (Figure 4), a behavior which is captured by our proxies (Figure 5).
3. This overestimation can be simply understood using the effective buoyancy formalism (Figure 6).

Although the hydrostatic system overestimates w_c, it is surprising how fine the resolution can become before this effect becomes appreciable. Figure 4 shows that differences between hydrostatic and nonhydrostatic solvers are virtually undetectable at resolutions of $dx = 2$ km or coarser. While this number is almost certainly dependent on one's model and the phenomena under consideration (W97 put this transition at 8 km rather than 2 km), it does at least point to the possibility of using hydrostatic models in the gray zone without substantial error.

While it is hoped that the results here provide some guidance for simulating in the gray zone, many questions and caveats still remain. For instance, although nonhydrostatic w_c seems to converge in Figure 4, the hydrostatic w_c does not. While surprising, this is consistent with the fact that D/H is not converged for either system (Figure 3c), and with the fact that $\sqrt{\beta_{nh}}$ is much less sensitive to D/H than $\sqrt{\beta_{hyd}}$ at $D/H \approx 1$ (Figure 5). Further increases in computational power and hence horizontal resolution should allow for a demonstration of convergence in D/H and hence also w_c for hydrostatic systems.

Also, equation (4) appears to explain why $dx = 250$ m marks the inner edge of the gray zone (consistent with Lebo & Morrison, 2015), but only does so in terms of H and n_{gray}. What sets the values of these numbers? We find $H \approx 500$ m, consistent with some recent studies (Hernandez-Deckers & Sherwood, 2016; Romps & Charn, 2015), but no established theory for parcel height currently exists. Furthermore, one might expect n_{gray} to be associated with the overall diffusivity of the dynamical variables, and hence to be highly model-dependent. Indeed, we were able to increase n_{gray} in FV^3 by a factor of 2–3 by simply increasing the divergence damping, which is a (hyper)-diffusion acting only on the divergent component of the flow (Zhao et al., 2012). Thus, while equation (4) may be diagnostically accurate, its predictive power may be limited by the need to diagnose H and n_{gray} for a given set of simulations.

Questions also remain regarding our simple scaling (13). This simple scaling ignores factors besides β which may change with resolution. For instance, attempts to fit w_c data from individual nonhydrostatic simulations to the "sticky" thermal model (12) yielded drag coefficients C_d which varied by over an order of magnitude across our resolution range. These drag coefficients may be a manifestation of the dynamic pressure force, whose resolution dependence we have neglected. Such variations in C_d do not render our scaling useless, but they do introduce error and hence limit the scaling's accuracy. Do such variations represent a real resolution-dependence of drag, or rather inaccuracies of the sticky thermal paradigm? Further work is needed to settle such questions.

Appendix A: Derivation of Analytical Solutions for β

We seek here solutions to equations (6) and (8) for the source B field (9).

We begin with the hydrostatic case. The p_{hyd} field associated with (9) for $z < H$ is given by

$$p_{\text{hyd}}(\mathbf{x}) = \int_z^\infty \rho_0 g \, dz' - \rho_0 B_0 (H - z) \cos\left(\frac{\pi x}{D}\right) \cos\left(\frac{\pi y}{D}\right). \tag{A1}$$

The hydrostatic effective buoyancy β_{hyd} can be obtained by direct substitution of (A1) into equation (8) and integration. The result is

$$\beta_{\text{hyd}}(\mathbf{x}) = 2\pi^2 B_0 \frac{zH}{D^2} \left(1 - \frac{z}{2H}\right) \cos\left(\frac{\pi x}{D}\right) \cos\left(\frac{\pi y}{D}\right). \tag{A2}$$

To obtain the nonhydrostatic β_{nh}, we make the ansatz

$$\beta_{\text{nh}}(\mathbf{x}) = \tilde{\beta}(z) \cos\left(\frac{\pi x}{D}\right) \cos\left(\frac{\pi y}{D}\right)$$

and substitute into (6) to obtain

$$-\partial_z{}^2 \tilde{\beta} + \frac{2\pi^2}{D^2} \tilde{\beta} = \begin{cases} 0 & z > H \\ \dfrac{2\pi^2}{D^2} B_0 & z < H \end{cases}. \tag{A3}$$

(A3) This is a second-order, constant coefficient, linear ordinary differential equation which is amenable to solution by standard textbook methods (which include invoking continuity of β and $\partial_z \beta$ at $z = H$, which can be derived from (6)). The result for $\tilde{\beta}$ is

$$\tilde{\beta}(z) = \begin{cases} B_0 \left[\cosh\left(\dfrac{\sqrt{2}\pi H}{D}\right) - 1\right] e^{-\frac{\sqrt{2}\pi z}{D}} & z > H \\ B_0 \left[\left(1 - e^{-\frac{\sqrt{2}\pi H}{D}}\right) \sinh\left(\dfrac{\sqrt{2}\pi z}{D}\right) - \cosh\left(\dfrac{\sqrt{2}\pi z}{D}\right) + 1\right] & z < H \end{cases}. \tag{A4}$$

With these solutions to equations (6) and (8) in hand, we now evaluate them at cylinder's center $\mathbf{x} = (0, 0, H/2)$ to obtain characteristic values for β_{nh} and β_{hyd} as a function of B_0, D, and H:

$$\beta_{\text{nh}} = B_0 \left[1 - \frac{1}{2} e^{-\frac{\pi H}{\sqrt{2}D}} \left(3 - e^{-\frac{\sqrt{2}\pi H}{D}}\right)\right]$$

$$\beta_{\text{hyd}} = B_0 \frac{3\pi^2}{4} \frac{H^2}{D^2}$$

These are equation (10) in the main text.

Appendix B: Comparison with Other Scalings

Previous authors have developed vertical velocity scalings analogous to ours. We focus here on the scalings of M16 (equation (27)), Pauluis and Garner (2006) (hereafter PG06, equation 19), and W97 (equation (4)), which in our notation are

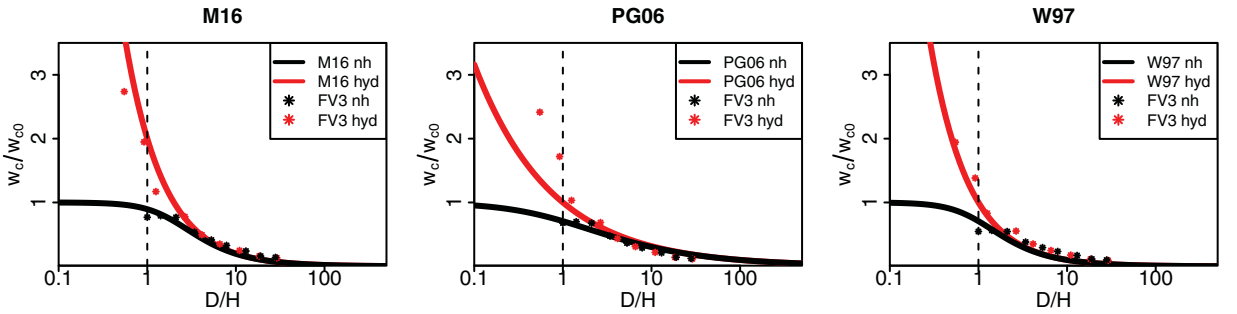

Figure B1. As in Figure 5, but for the scalings in equation (B1).

$$\text{M16}: \quad \frac{w_c}{w_{c0}} = \frac{1}{\sqrt{1+D^2/4H^2}}$$

$$\text{PG06}: \quad \frac{w_c}{w_{c0}} = \frac{1}{\sqrt{1+D/H}} \tag{B1}$$

$$\text{W97}: \quad \frac{w_c}{w_{c0}} = \frac{1}{\sqrt{1+D^2/H^2}}\,.$$

Here we have set the α parameter of M16 equal to $1/\sqrt{2}$ (right in the 0.5–1 range used in Morrison (2016b)). All three of these studies point out that the "1" in the denominator in their expressions comes from nonhydrostatic effects, so hydrostatic versions of these expressions can be obtained by simply omitting this "1."

The plots of Figure B1 show the analogs of Figure 5, but for the above scalings (we recalculate w_{c0} for each plot by least squares fit to the nonhydrostatic data, as in Figure 5). These scalings are qualitatively similar to each other and to equation (13), and the M16 and W97 scalings bear a particularly close relation to ours as all three vary as H/D in the hydrostatic limit. The PG06 scaling varies as $\sqrt{H/D}$ in this limit, giving it a slightly different shape that seems to be a poorer match to the FV^3 data, for both the hydrostatic and nonhydrostatic cases. The W97 scaling slightly underestimates w_c throughout the gray zone but does well in capturing the hydrostatic overestimation in the convection-resolving regime, and the M16 scaling does quite well across the board.

Appendix C: Parcel Diagnostics

To diagnose average values of D, H, and w_c across parcels in a given simulation, we devised an algorithm to automatically detect convecting parcels in 3-D snapshot output and then diagnose these quantities individually for each parcel. Averaging over parcels within a given simulation then yields the data plotted in Figures 3, 5, and Figures B1 and C1. This appendix describes this diagnostic algorithm in detail.

For a given run, we analyze daily snapshots from the last 20 days of the run. In a given snapshot, we locate parcels by finding the global maximum $w_{\max}$ of w. This maximum is discarded if it lies within three grid cells of the horizontal boundaries (for ease of analysis), or if its pressure is lower than 250 hPa, since such maxima correspond to tall, rare plumes that are often comprised of multiple distinct parcels which are difficult to analyze and not representative of typical convecting parcels. If $w_{\max}$ is not discarded we then record its horizontal position $(i_{\max}, j_{\max})$, and search for the center of the corresponding density anomaly (typically located higher than $w_{\max}$) by maximizing $B(i_{\max}, j_{\max}, k)$ in the vertical index k. In searching for this $k_{\max}$ we exclude boundary-layer points at pressures higher than $p_{\text{bl}}=950$ hPa (to avoid surface-induced buoyancy maxima), and also exclude stratospheric points at pressure lower than $p_{\text{strat}}=150$ hPa (to avoid gravity-wave related buoyancy maxima). To ensure that the buoyancy maximum $B_{\max}$ at the resulting $k_{\max}$ is indeed associated with $w_{\max}$, we discard parcels where the distance between $k_{\max}$ and $w_{\max}$ is greater than 2000 m. With $B_{\max}$ so located, we then impose a "cloud-core" condition of $w_{\max} > 0.5$ m/s, $q_n(i_{\max}, j_{\max}, k_{\max}) > 1\times$

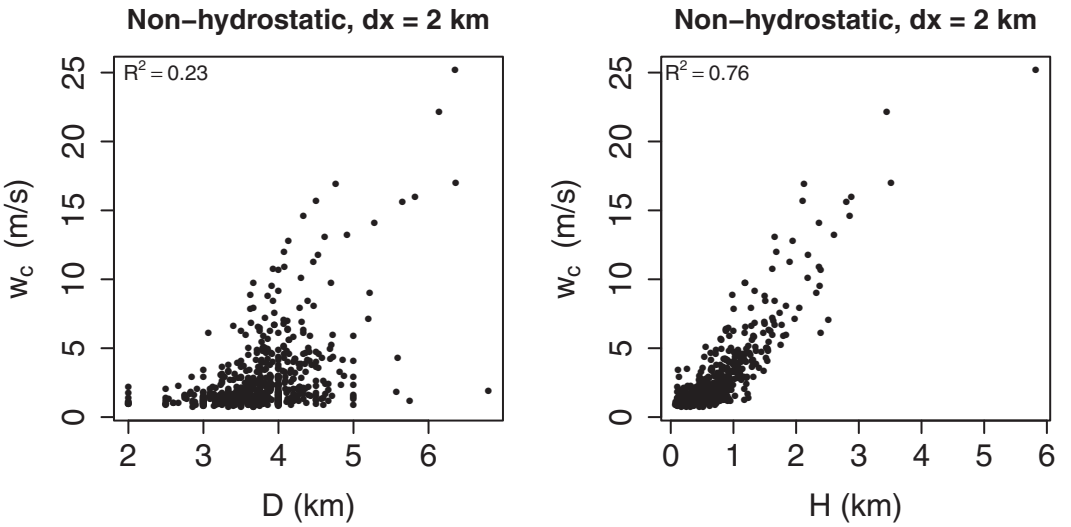

Figure C1. Scatterplots of w_c versus (left) D and (right) H for all parcels identified in the nonhydrostatic, $dx = 2$ km simulation. Note the relatively large spreads in w_c and H, relative to D. Also note the high correlation between w_c and H. See text for further discussion.

10^{-5} kg/kg (where q_n is nonprecipitating condensate), and $B_{max} > B_{thresh}$, where the latter is resolution-dependent and is given by

$$B_{thresh}(dx) = 0.01 + 0.03\frac{\ln(dx/0.125\,\text{km})}{\ln 64}\ . \ (\text{m/s}^2) \tag{C1}$$

This gives a factor of 4 increase in B_{thresh} that is linear in log dx, which is just how the average parcel B_{max} values behave across resolution (not shown). This functional form for B_{thresh} prevents changes in average B_{max} with resolution from unduly affecting our diagnoses. Any parcel not meeting the cloud-core condition is discarded.

If not discarded, the parcel is now considered to be based at $(i_{max}, j_{max}, k_{max})$, and we diagnose its vertical extent by marching upwards and downwards from k_{max} until $B < B_{thresh}$. This yields indices k_{top} and k_{bot} for parcel top and bottom. We then check that $p(k_{top}) > p_{strat}$ and $p(k_{bot}) < p_{bl}$, and discard the parcel if those conditions are not met. If they are, we proceed to diagnose the parcel's height as the sum of grid box heights from k_{bot} to k_{top}. We then diagnose parcel diameter by, for each $k \in [k_{bot}, k_{top}]$, finding the largest contiguous range of i, including i_{max}, such that $B(i, j_{max}, k) > B_{thresh}$. Multiplying the number of i values in this range by dx then gives an estimate of the parcel's diameter at level k. This can be repeated for all $k \in [k_{bot}, k_{top}]$, as well as by looking at parcel extent in j rather than i. A simple averaging of all these values then yields the parcel's diameter D. We set the parcel's $w_c = w_{max}$. We then "erase" this parcel from the 3-D w field by setting $w(i, j, k) =$ NA for all k and all i, j within 3 of i_{max} and j_{max}. We then search for the next w maxima in this modified w field, and repeat the above processes. This algorithm repeats until 100 w maxima in a given snapshot have been identified and either discarded or had their properties fully diagnosed, or until the number of discarded parcels exceeds 25, whichever comes first. The next snapshot is then processed in the same manner. This procedure, while crude, is computationally efficient and also suffices to yield several hundred parcels for each simulation. Average values of all diagnostics for a given simulation are then computed as simple averages over all parcels from all snapshots.

To get a feel for the statistics of a given simulation, Figure C1 shows scatterplots of w_c versus D and w_c versus H for all 621 parcels identified from the nonhydrostatic, 2 km simulation. Note that D has a fairly symmetric distribution and an unremarkable spread, whereas H and w are highly skewed, with outliers roughly an order of magnitude larger than their means (the means of H and w_c being 750 m and 2.7 m/s, respectively). Most notably, w_c and D appear more or less uncorrelated, whereas there is a strong relationship between w_c and H ($R^2 = 0.77$). Though this might be expected from equation (10a), we cannot rule out feedbacks that elongate parcels which have higher w_c (for instance, because higher w_c implies higher vertical

w gradients, and hence possibly more horizontal convergence and entrainment, adding mass and possibly height to the plume). Thus, the strong correlation between w_c and H should not be interpreted as causation from H to w_c, but should rather be regarded as an intriguing relationship worthy of further study.

Acknowledgments
The author thanks Leo Donner and Isaac Held for guidance, Usama Anber for FV^3 orientation, and S-J Lin and especially Lucas Harris for assistance in configuring FV^3 to run at these relatively high resolutions. Thanks are also due to Leo Donner, Yi Ming, Lucas Harris, Steven Garner, and especially Jacob Seeley for commenting on drafts of this work. Special thanks are due to Ming Zhao for asking how effective buoyancy behaves in a hydrostatic model, which question initiated this study. Simulations were run on the Gaea supercomputer at Oak Ridge National Laboratory, Oak Ridge, Tennessee. The author is supported by the Visiting Scientist Program of the Princeton Atmosphere and Ocean Science program. Data and analysis scripts for this study (in R) are available at https://github.com/jeevanje/w_hydrostatic.

References

Adcroft, A., Dutkiewicz, S., Ferreira, D., Heimbach, P., Jahn, O., & Maze, G. (2011). *MITgcm user manual* (Tech. Rep.). Cambrigde MA: Massachusetts Institute of Technology (MIT). Retrieved from http://mitgcm.org/sealion/online_documents/manual.pdf

Arakawa, A., & Schubert, W. H. (1974). Interaction of a cumulus cloud ensemble with the large-scale environment, Part I. *Journal of the Atmospheric Sciences*, *31*, 674–701. https://doi.org/10.1175/1520-0469(1974)031<0674:IOACCE>2.0.CO;2

Bryan, G. H., & Morrison, H. (2011). Sensitivity of a simulated squall line to horizontal resolution and parameterization of microphysics. *Monthly Weather Review*, *140*(1), 202–225. https://doi.org/10.1175/MWR-D-11-00046.1

Bryan, G. H., Wyngaard, J. C., & Fritsch, J. M. (2003). Resolution requirements for the simulation of deep moist convection. *Monthly Weather Review*, *131*(10), 2394–2416. https://doi.org/10.1175/1520-0493(2003)131<2394:RRFTSO>2.0.CO;2

Chen, J. H., & Lin, S. J. (2013). Seasonal predictions of tropical cyclones using a 25-km-resolution general circulation model. *Journal of Climate*, *26*(2), 380–398. https://doi.org/10.1175/JCLI-D-12-00061.1

Das, P. (1979). A non-Archimedean approach to the equations of convection dynamics. *Journal of Atmospheric Sciences*, *36*(11), 2183–2190. https://doi.org/10.1175/1520-0469(1979)036<2183:ANAATT>2.0.CO;2

Davies-Jones, R. (2003). An expression for effective buoyancy in surroundings with horizontal density gradients. *Journal of the Atmospheric Sciences*, *60*(23), 2922–2925. https://doi.org/10.1175/1520-0469(2003)060<2922:AEFEBI>2.0.CO;2

Donner, L. J., O'brien, T. A., Rieger, D., Vogel, B., & Cooke, W. F. (2016). Are atmospheric updrafts a key to unlocking climate forcing and sensitivity? *Atmospheric Chemistry and Physics*, *16*(20), 12,983–12,992. https://doi.org/10.5194/acp-16-12983-2016

Harris, L. M., & Lin, S.-J. (2013). A two-way nested global-regional dynamical core on the cubed-sphere grid. *Monthly Weather Review*, *141*(1), 283–306. https://doi.org/10.1175/MWR-D-11-00201.1

Hernandez-Deckers, D., & Sherwood, S. C. (2016). A numerical investigation of cumulus thermals. *Journal of the Atmospheric Sciences*, *73*(10), 4117–4136. https://doi.org/10.1175/JAS-D-15-0385.1

Jeevanjee, N., Hassanzadeh, P., Hill, S., & Sheshadri, A. (2017). A perspective on climate model hierarchies. *Journal of Advances in Modeling Earth Systems*, *9*, 1760–1771. https://doi.org/10.1002/2017MS001038

Jeevanjee, N., & Romps, D. M. (2015). Effective buoyancy, inertial pressure, and the mechanical generation of boundary layer mass flux by cold pools. *Journal of the Atmospheric Sciences*, *72*(8), 3199–3213. https://doi.org/10.1175/JAS-D-14-0349.1

Jeevanjee, N., & Romps, D. M. (2016). Effective buoyancy at the surface and aloft. *Quarterly Journal of the Royal Meteorological Society*, *142*, 811–820. https://doi.org/10.1002/qj.2683

Kain, J. S., Weiss, S. J., Bright, D. R., Baldwin, M. E., Levit, J. J., Carbin, G. W., . . . Thomas, K. W. (2008). Some practical considerations regarding horizontal resolution in the first generation of operational convection-allowing NWP. *Weather and Forecasting*, *23*(5), 931–952. https://doi.org/10.1175/WAF2007106.1

Kato, T., & Saito, K. (1995). Hydrostatic and non-hydrostatic simulations of moist convection. *Journal of the Meteorological Society of Japan. Series II*, *73*(1), 59–77. https://doi.org/10.2151/jmsj1965.73.1_59

Lean, H. W., Clark, P. A., Dixon, M., Roberts, N. M., Fitch, A., Forbes, R., & Halliwell, C. (2008). Characteristics of high-resolution versions of the met office unified model for forecasting convection over the United Kingdom. *Monthly Weather Review*, *136*(9), 3408–3424. https://doi.org/10.1175/2008MWR2332.1

Lebo, Z. J., & Morrison, H. (2015). Effects of horizontal and vertical grid spacing on mixing in simulated squall lines and implications for convective strength and structure. *Monthly Weather Review*, *143*, 4355–4375. https://doi.org/10.1175/MWR-D-15-0154.1

Lin, S.-J. (2004). A 'vertically Lagrangian' finite-volume dynamical core for global models. *Monthly Weather Review*, *132*(10), 2293–2307. https://doi.org/10.1175/1520-0493(2004)132<2293:AVLFDC>2.0.CO;2

Markowski, P., & Richardson, Y. (2011). *Mesoscale meteorology in midlatitudes* (430. pp.). West Sussex, UK: John Wiley.

Morrison, H. (2016a). Impacts of updraft size and dimensionality on the perturbation pressure and vertical velocity in cumulus convection. Part I: Simple, generalized analytic solutions. *Journal of the Atmospheric Sciences*, *73*(4), 1441–1454. https://doi.org/10.1175/JAS-D-15-0041.1

Morrison, H. (2016b). Impacts of updraft size and dimensionality on the perturbation pressure and vertical velocity in cumulus convection. Part II: Comparison of theoretical and numerical solutions and fully dynamical simulations. *Journal of the Atmospheric Sciences*, *73*(4), 1455–1480. https://doi.org/ 10.1175/JAS-D-15–0041.1

Noda, A. T., Satoh, M., Yamada, Y., Kodama, C., & Seiki, T. (2014). Responses of tropical and subtropical high-cloud statistics to global warming. *Journal of Climate*, *27*(20), 7753–7768. https://doi.org/10.1175/JCLI-D-14-00179.1

Orlanski, I. (1981). The quasi-hydrostatic approximation. *Journal of the Atmospheric Sciences*, *38*(3), 572–582. https://doi.org/10.1175/1520-0469(1981)038<0572:TQHA>2.0.CO;2

Pauluis, O., & Garner, S. (2006). Sensitivity of radiative convective equilibrium simulations to horizontal resolution. *Journal of the Atmospheric Sciences*, *63*(7), 1910–1923. https://doi.org/10.1175/JAS3705.1

Prein, A. F. (2015). A review on regional convection-permitting climate modeling: Demonstrations, prospects, and challenges. *Reviews of Geophysics*, *53*, 323–361. https://doi.org/10.1002/2014RG000475

Putman, W. M., & Suarez, M. (2011). Cloud-system resolving simulations with the NASA Goddard Earth Observing System global atmospheric model (GEOS-5). *Geophysical Research Letters*, *38*, L16809. https://doi.org/10.1029/2011GL048438

Romps, D. M. (2008). The dry-entropy budget of a moist atmosphere. *Journal of the Atmospheric Sciences*, *65*(12), 3779–3799. https://doi.org/10.1175/2008JAS2679.1

Romps, D. M., & Charn, A. B. (2015). Sticky thermals: Evidence for a dominant balance between buoyancy and drag in cloud updrafts. *Journal of the Atmospheric Sciences*, *72*(8), 2890–2901. https://doi.org/10.1175/JAS-D-15-0042.1

Scorer, R. S. (1957). Experiments on convection of isolated masses of buoyant fluid. *Journal of Fluid Mechanics*, *2*, 583–594. https://doi.org/10.1017/S0022112057000397

Sherwood, S. C., Hernández-Deckers, D., Colin, M., & Robinson, F. (2013). Slippery thermals and the cumulus entrainment paradox*. *Journal of the Atmospheric Sciences*, *70*(8), 2426–2442. https://doi.org/10.1175/JAS-D-12-0220.1

VandenBerg, M. A., Coniglio, M. C., & Clark, A. J. (2014). Comparison of next-day convection-allowing forecasts of storm motion on 1- and 4-km grids. *Weather and Forecasting*, *29*(4), 878–893. https://doi.org/10.1175/WAF-D-14-00011.1

Wehner, M. F., Reed, K. A., Li, F., Bacmeister, P. J., Chen, C. T., Paciorek, C., . . . Jablonowski, C. (2014). The effect of horizontal resolution on simulation quality in the Community Atmospheric Model, CAM5.1. *Journal of Advances in Modeling Earth Systems*, *6*, 980–997. https://doi.org/10.1002/2013MS000276

Weisman, M. L., Skamarock, W. C., & Klemp, J. B. (1997). The resolution dependence of explicitly modeled convective systems. *Monthly Weather Review*, *125*(4), 527–548. https://doi.org/10.1175/1520-0493(1997)125<0527:TRDOEM>2.0.CO;2

Woodward, B. (1959). The motion in and around isolated thermals. *Quarterly Journal of the Royal Meteorological Society*, *85*, 144–151.

Wyngaard, J. C. (2004). Toward numerical modeling in the Terra Incognita. *Journal of the Atmospheric Sciences*, *61*(14), 1816–1826. https://doi.org/10.1175/1520-0469(2004)061<1816:TNMITT>2.0.CO;2

Zhao, M., Held, I. M., & Lin, S.-J. (2012). Some counterintuitive dependencies of tropical cyclone frequency on parameters in a GCM. *Journal of the Atmospheric Sciences*, *69*(7), 2272–2283. https://doi.org/10.1175/JAS-D-11-0238.1